

Article

A Wind Tunnel Test of the Anti-Icing Properties of MoS₂/ZnO Hydrophobic Nano-Coatings for Wind Turbine Blades

Bo Liu¹, Zhiyuan Liu¹, Yan Li^{1,2,*} and Fang Feng^{2,3,*} ¹ College of Engineering, Northeast Agricultural University, Harbin 150030, China² Key Laboratory of Icing and Anti/De-Icing, China Aerodynamics Research and Development Center, Mianyang 621000, China³ College of Arts and Sciences, Northeast Agricultural University, Harbin 150030, China

* Correspondence: liyanneau@neau.edu.cn (Y.L.); fengfang@neau.edu.cn (F.F.)

Abstract: Wind turbines operating in cold regions are prone to blade icing, which seriously affects their aerodynamic characteristics and safety performance. Coatings are one of the effective solutions to the icing problem on wind turbine blades. In this study, MoS₂/ZnO/PDMS superhydrophobic nano-anti-icing coatings were prepared using the hydrothermal method and the liquid phase method. SEM revealed that the MoS₂/ZnO coating was a typical superhydrophobic nanostructure with an ultra-thin sheet-like morphology of clusters and a hilly nano-rough structure, with contact angles (CA) of 152.1° and 4.7° with water droplets and the sliding angle (SA), respectively. The MoS₂/ZnO/PDMS coating had an adhesion strength to ice of 78 kPa, which was 60.2% lower than an uncoated surface. The icing effects of the NACA0018 airfoil blade model with or without MoS₂/ZnO coatings were studied at different ambient temperatures and wind speeds using the icing wind tunnel test. The results showed that, compared to uncoated blades, the level of icing was lower on the blade airfoil surface that was coated with MoS₂/ZnO. At 10 m/s and −10 °C, the icing thickness and icing area of the leading edge of the blade airfoil were 13.7% and 28.3% lower, respectively. This study provides a valuable reference for the development of anti-icing coatings for wind turbine blades.

Keywords: anti-icing; hydrophobic coating; MoS₂/ZnO; wind turbine blade; wind tunnel test



Citation: Liu, B.; Liu, Z.; Li, Y.; Feng, F. A Wind Tunnel Test of the Anti-Icing Properties of MoS₂/ZnO Hydrophobic Nano-Coatings for Wind Turbine Blades. *Coatings* **2023**, *13*, 686. <https://doi.org/10.3390/coatings13040686>

Academic Editor: Alexandra Muñoz-Bonilla

Received: 16 February 2023

Revised: 20 March 2023

Accepted: 22 March 2023

Published: 27 March 2023



Copyright: © 2023 by the authors. Licensee MDPI, Basel, Switzerland. This article is an open access article distributed under the terms and conditions of the Creative Commons Attribution (CC BY) license (<https://creativecommons.org/licenses/by/4.0/>).

1. Introduction

With the depletion of fossil energy resources, the demand for renewable energy is increasing. Notably, wind energy has become a popular option globally because of its wide distribution, great developmental potential, and environmental friendliness [1–4]. Worldwide, high-quality wind energy resources are mainly distributed in high latitudes, and high-altitude cold regions of the Northern Hemisphere [5]. However, as global climate change has intensified and extreme climates have become more frequent, wind turbines in these regions are at risk of blade icing, which reduces their aerodynamic performance and power generation efficiency. Blade icing also affects the safe operation of the system and increases maintenance costs [6–8]. Therefore, preventing or reducing blade surface icing on wind turbines has become a serious challenge in many engineering fields.

At present, anti-icing and de-icing technologies for wind turbine blades are divided into active and passive methods [9,10]. Active methods, such as the mechanical de-icing method, the thermal de-icing method, and the ultrasonic vibration de-icing methods, are often costly, energy intensive, less efficient, and short-lived, and they often require special equipment, all of which makes them less practical for engineering applications [11–14]. As a result, scholars have gradually shifted their focus from active de-icing to passive anti-icing [15]. The passive method uses the hydrophobic properties of certain materials to reduce the adhesion between the water droplets and the coating surface. Owing to these superhydrophobic properties, water droplets easily roll off the coating surface under the action of external natural forces, greatly reducing the accumulation of liquid water on the

surface of the structure and providing good waterproofing performance. This reduces the amount of ice on the surface of the material and achieves the anti-icing effect [16,17]. Due to the wettability of superhydrophobic materials, their applications in wind turbine anti-icing are very broad, and they have become a popular research topic in wind turbine anti-icing.

In recent years, with the development of nanotechnology, transition metal sulfides with layered structures have become a trend in research [18]. In particular, compared with bulk materials, nanoscale MoS₂ exhibits unique characteristics, including reduced surface friction, making it a valuable nanomaterial for use in optics, electronics, new energy, and other fields [19]. For example, Zhang proposed a simple and feasible method for MoS₂ modification [20]. The coating has excellent self-cleaning ability, chemical durability, wear resistance and corrosion resistance. At the same time, ZnO is a versatile inorganic semiconductor material with a simple preparation process and rich and varied morphology, and it produces micro-nano structures with low surface energy. It is widely used in gas sensing, energy storage devices, and antibacterial, photocatalytic, biomedical, and hydrophobic coatings. With the development of composite technology, ZnO particles are favored because of their ability to improve the properties of composite materials [21]. With the development of nanotechnology, the combination of two kinds of materials with their own advantages can often play a better synergistic role and show more excellent properties.

In this study, to prepare the MoS₂/ZnO nanomaterial superhydrophobic coating, ZnO was loaded onto the surface of MoS₂ nanosheets using the hydrothermal method and the liquid phase method. These methods have the advantages of simple processes, low production costs, and high yield, and they can produce crystals with complete grain, small grain size, and uniform grain structure, which is suitable for spraying on large blades in actual industrial production [22,23]. The hydrophobic and anti-icing properties of the synthesized MoS₂/ZnO nanomaterials were investigated. Their chemical composition and microstructure were characterized using X-ray photoelectron spectroscopy (XPS) and scanning electron microscopy (SEM). The hydrophobicity and icing adhesion strength were measured using a contact angle (CA) measuring instrument and a static anti-icing test. Finally, the wind tunnel test was used to evaluate the anti-icing effect of the MoS₂/ZnO nanomaterial superhydrophobic coating based on icing shape, icing area, and leading-edge icing thickness. The development of MoS₂/ZnO nano-superhydrophobic materials in this study has an important reference value for research in blade anti-icing.

2. Test Materials and Methods

2.1. Materials and Preparation

The reagents required for the tests and corresponding manufacturers are shown in Table 1.

Table 1. Test reagents and manufacturers.

Reagent Name	Grade	Manufacturer
Ammonium molybdate ($(\text{NH}_4)_6\text{Mo}_7\text{O}_{24}\cdot 4\text{H}_2\text{O}$)	Analytical reagent (AR)	Tianjin Hengxin Chemical Co., Ltd., Tianjin, China
Thiourea (H_2NCSNH_2)	AR	Tianjin Tianli Chemical Reagent Co., Ltd., Tianjin, China
Zinc acetate ($\text{Zn}(\text{CH}_3\text{COO})_2\cdot 2\text{H}_2\text{O}$)	AR	Tianjin Tianli Chemical Reagent Co., Ltd.
Lithium hydroxide ($\text{LiOH}\cdot \text{H}_2\text{O}$)	AR	Tianjin Fuchen Chemical Reagent Factory, Tianjin, China
Absolute alcohol ($\text{CH}_3\text{CH}_2\text{OH}$)	AR	Tianjin Fuyu Fine Chemical Co., Ltd., Tianjin, China
Polydimethylsiloxane (PDMS, Sylgard 184 base and curing agent)	AR	American Dow Corning Company, Midland, MI, USA
n-hexane (C_6H_{14})	AR	Tianjin Fuyu Fine Chemical Co., Ltd., Tianjin, China

(1) Preparation of MoS₂ nanomaterials

First, 2.47 g of ammonium molybdate and 4.56 g of thiourea were rapidly dissolved in 70 mL of distilled water and stirred for 30 min to obtain a uniform and transparent solution. The solution was then transferred to a high-pressure reactor at 180 °C for 24 h. The high-pressure reactor was cooled to room temperature to collect the precipitate, which was centrifuged at 5000 r/min for 3 min, washed with distilled water, treated with anhydrous ethanol to a neutral pH, and finally dried in a vacuum at 60 °C for 24 h. The dried powder was ground to obtain MoS₂ nanosheets.

(2) Preparation of MoS₂/ZnO nanomaterials

In this process, 7 g of zinc acetate was rapidly dispersed and reacted in 230 mL of anhydrous ethanol in a water bath at a constant temperature of 80 °C for 10 min. Subsequently, 2 g of lithium hydroxide was added and sonicated at room temperature until the mixture was completely dissolved. In addition, 0.15 g of MoS₂ nanosheets were added to 20 mL of anhydrous ethanol, and the mixture was ultrasonically dispersed at room temperature until uniformly dispersed. This solution was then added to the first solution, ultrasonically dispersed for 20 min, and then stirred at room temperature for 2 h. The precipitate was centrifuged at 5500 r/min for 5 min at room temperature and washed twice with anhydrous ethanol. Finally, the solid mixture was dried in a vacuum at 40 °C for 24 h and ground to obtain MoS₂/ZnO nanomaterials.

2.2. Preparation of Coating

A NACA0018 airfoil glass fiber-reinforced plastic blade (GFRP blade) with a chord length of 100 mm and a span height of 20 mm was selected as a test piece. The blade model schematic and physical diagram are shown in Figure 1. The GFRP blade was ultrasonically cleaned with anhydrous ethanol ultrasonic for 10 min, rinsed with deionized water, and allowed to dry. Meanwhile, the PDMS precursor was mixed with the PDMS curing agent at a ratio of 10:1 to obtain the PDMS adhesive [24,25]. Subsequently, 1 g of the PDMS mixture was added to 50 mL of n-hexane while stirring at room temperature for 10 min. An equivalent mass of MoS₂/ZnO nanomaterials was added and stirred for 30 min to form a uniformly mixed suspension, which was then evenly sprayed on the blade surface using a spray gun held 15 cm away from the blade. The GFRP blade was then cured in an oven at 60 °C for 12 h to obtain the MoS₂/ZnO/PDMS nanomaterial superhydrophobic coated blade. The MoS₂/PDMS nano-coating was prepared via a similar process.

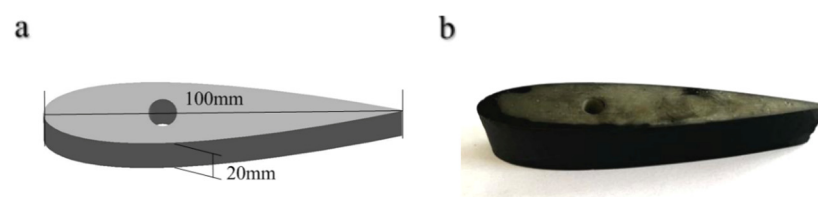


Figure 1. Test blade model with NACA0018 airfoil (a) schematic diagram and (b) photo.

2.3. Testing and Characterization

XPS analysis: The elemental composition and electronic energy state of the material surface were determined using X-ray photoelectron spectroscopy (ESCALAB 250 Xi; ThermoFisher, Waltham, MA, USA).

SEM analysis: The surface morphology of the prepared material was analyzed using a field emission scanning electron microscope (SU8010; Hitachi, Tokyo, Japan).

Wetting performance test: The water contact angle (CA) and sliding angle (SA) of the sample were measured using an optical contact angle measuring instrument (JCD2000D3M; Shanghai Zhongchen Digital Technology Instrument Co., Ltd., Shanghai, China) with 5 µL deionized water.

Surface roughness test: The average surface roughness (Ra) of the coating was characterized by an atomic force microscope (AFM, Dimension Edge, Billerica, MA, USA).

Ice adhesion strength test: A bottomless cylindrical ice sample with a bottom diameter of 25 mm and a height of 20 mm was filled with deionized water and frozen at $-20\text{ }^{\circ}\text{C}$ for 12 h. The frozen icicle was pushed with a digital dynamometer (Figure 2), and the maximum force (F_m in N) required to detach the icicle from the coating surface was recorded to calculate the adhesion strength of the ice using the following formula [26]:

$$\tau_{\text{ice}} = (F_m) / A_{\text{ice}} \quad (1)$$

where τ_{ice} (kPa) is the adhesion strength of the ice, F_m (N) is the maximum force required to detach the icicle from the coating surface, and A_{ice} (m^2) is the bottom area of the icicle.



Figure 2. Photo of the digital dynamometer.

2.4. Anti-Icing Test in the Icing Wind Tunnel

The anti-icing test in the icing wind tunnel was completed in a recirculating low-temperature icing wind tunnel at the wind energy research laboratory of Northeast Agricultural University. The ice wind tunnel test took place in October 2022. The recirculating icing wind tunnel test system consisted of a refrigeration system, a spray system, and an air duct (Figure 3). The size of the wind tunnel test section was $250\text{ mm} \times 250\text{ mm}$, and the nozzle was located at the center of the stable section of the air duct. A spray system pressurized the air to 4 MPa. The test blade sample was fixed on the fixed frame of the test section, with a blocking area ratio (blade to fixed frame) of about 1.8%. The specifications of the test section met the test requirements for the anti-icing test.

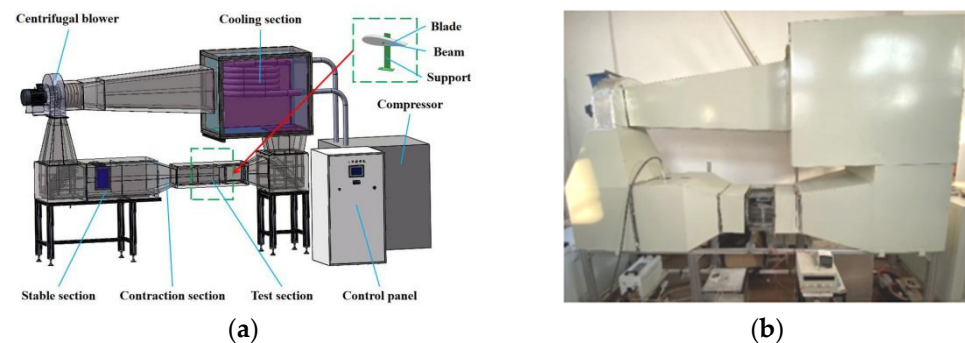


Figure 3. Icing wind tunnel test system (a) schematic diagram and (b) photo.

The liquid water content (LWC) of the icing wind tunnel test section was calibrated by the grid method. The LWC was calculated according to the icing condition of the grid combined with the LWC formula [27]:

$$LWC = \frac{\rho_{\text{ice}} \times h_i}{v} \quad (2)$$

where ρ_{ice} is the ice density, h_i is the ice thickness on the grid, and v is the ambient wind speed. The calibration results of LWC are shown in Figure 4. In the central area of the icing wind tunnel test section, the distribution of liquid water content was relatively uniform, and the scale of this area met the test requirements.

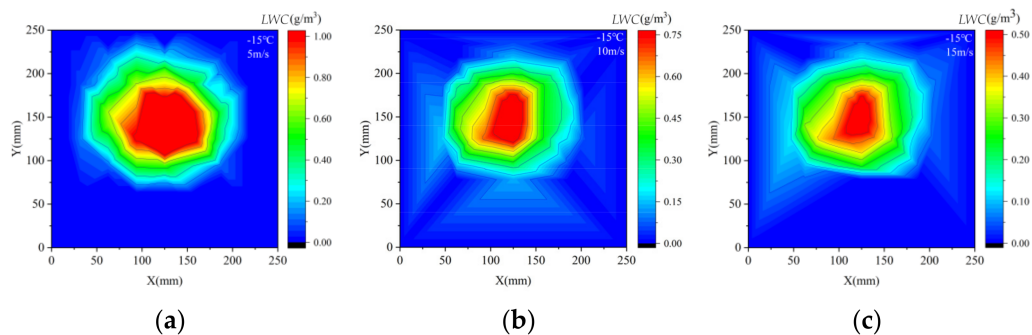


Figure 4. The calibration results of LWC. (a) 5 m/s, (b) 10 m/s, (c) 15 m/s.

2.5. Test Scheme

To study the anti-icing effects of the MoS₂/PDMS nano-coating and the MoS₂/ZnO/PDMS nano-coating on the surface of wind turbine blades, three temperature conditions (−5 °C, −10 °C, and −15 °C), three wind speeds (5 m/s, 10 m/s, and 15 m/s), and an icing time of 3 min were selected in this experiment. The anti-icing effects of the MoS₂/PDMS nano-coating and the MoS₂/ZnO/PDMS composite nano-coating were studied by examining the icing distribution on the surface of blades. The test scheme is shown in Table 2.

Table 2. Icing wind tunnel test scheme.

Test Conditions	Ambient Temperature (°C)	Liquid Water Content (g/m ³)	Water Droplet Diameter (µm)	Wind Velocity (m/s)	Time (min)
1	−5	0.5~1	50~70	5	3
2				10	
3				15	
4	−10			5	
5				10	
6				15	
7	−15			5	
8				10	
9				15	

3. Results and Discussion

3.1. X-ray Photoelectron Spectroscopy Analysis

To determine the surface chemical composition and valence state of the MoS₂/ZnO nanomaterials, the MoS₂ nanomaterials and MoS₂/ZnO nanomaterials were analyzed using XPS. A high-resolution XPS diagram of the Mo3d orbital of the MoS₂ nanosheets is shown in Figure 5a. Two peaks were obtained at 231.9 eV and 228.7 eV in the Mo3d orbital of the MoS₂ nanosheets, which corresponded to Mo⁴⁺. A high-resolution XPS diagram of the Mo3d orbital of the MoS₂/ZnO nanomaterials is shown in Figure 5c. The XPS results show that after the growth of ZnO nanoparticles, compared with pure MoS₂ nanosheets, the two peaks of Mo⁴⁺ shifted to a higher binding energy of about 0.3 eV, indicating electron transfer from MoS₂ to ZnO and proving the successful synthesis of the MoS₂/ZnO nanomaterials. The results also show two peaks at 235.6 eV and 232.5 eV, corresponding to Mo⁶⁺, which suggests that there was oxidation of the surface of the MoS₂ nanosheets. In addition, a peak can also be observed at 226.0 eV, which corresponds to the 2s orbital of the S. In Figure 5b, two peaks of the MoS₂ nanosheets can be observed at 161.6 eV and 162.9 eV, corresponding to the S 2p_{3/2} and S 2p_{1/2} orbitals, respectively, indicating that the S in the MoS₂ nanosheets had a valence state of −2, which is consistent with the standard

characteristic peak of S in the MoS₂ reported in the literature. Similarly, as demonstrated in Figure 5d, the XPS results for the MoS₂/ZnO nanomaterials were consistent with the results for MoS₂ nanosheets. In Figure 5e, two peaks can be observed at 1021.9 eV and 1044.9 eV, corresponding to the 2p_{3/2} and 2p_{1/2} orbitals of Zn²⁺. In Figure 5f, two peaks can be observed at 530.7 eV and 531.5 eV in the O 1s orbital, corresponding to the Zn-O and Mo-O bonds, respectively. According to the literature analysis, these peaks indicate the presence of Zn-O bonds and Mo-O bonds in the MoS₂/ZnO nanomaterials [28–31].

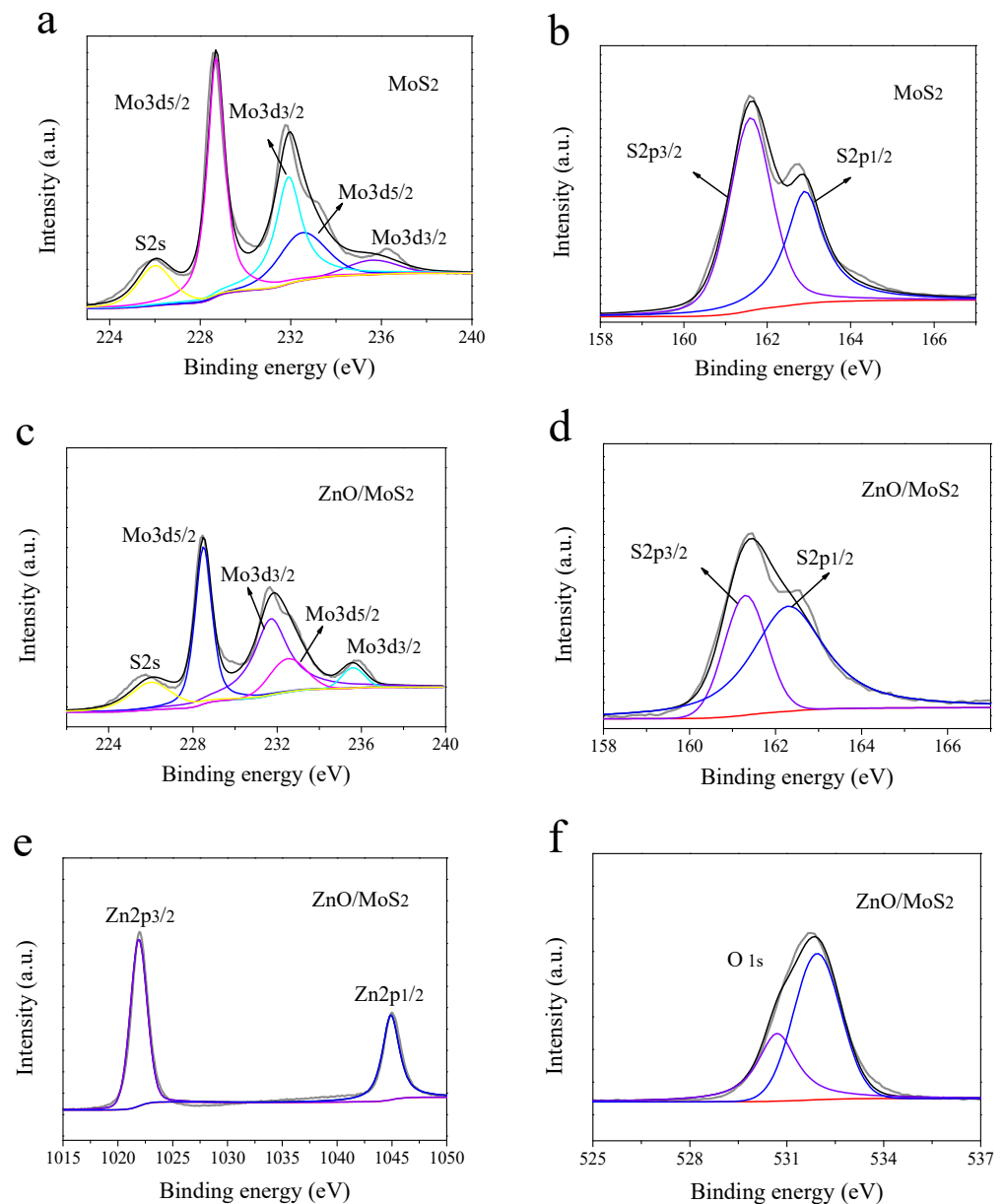


Figure 5. XPS spectra of the MoS₂ nanomaterial: (a) Mo 3d and (b) S 2p; XPS spectra of the MoS₂/ZnO nanomaterials: (c) Mo 3d, (d) S 2p, (e) Zn 2p, and (f) O 1s.

3.2. Microstructure Characterization of the Coating Surface

The SEM images allowed for close observation and analysis of the morphology and surface state of the prepared samples. The SEM image of the nanomaterials prepared using the above experimental method is shown in Figure 6. As demonstrated in Figure 6a, the MoS₂ was an ultra-thin and curly-layered nanosheet structure with a thickness of about 5 nm and a lateral length of about 190 nm. The nanosheets were uniform and closely arranged, with smooth surfaces and porous structures. The SEM image of the MoS₂/ZnO

nanomaterials is shown in Figure 6b. It shows that the MoS₂ still exhibited nanosheet morphology after the ZnO nanoparticles were loaded. In addition, compared with the MoS₂ nanosheets, the MoS₂/ZnO nanomaterials exhibited little change in lateral size. The surface roughness test results showed that the average surface roughness of the uncoated blade, the MoS₂ nano-coated blade, and the MoS₂/ZnO nano-coated blade were 1.71 nm, 16.74 nm, and 39.34 nm, respectively. The surface of the MoS₂/ZnO nanomaterials had a nano-rough structure, which resulted in the formation of a micro-nano rough structure in the coating surface, which is essential for constructing a superhydrophobic surface.

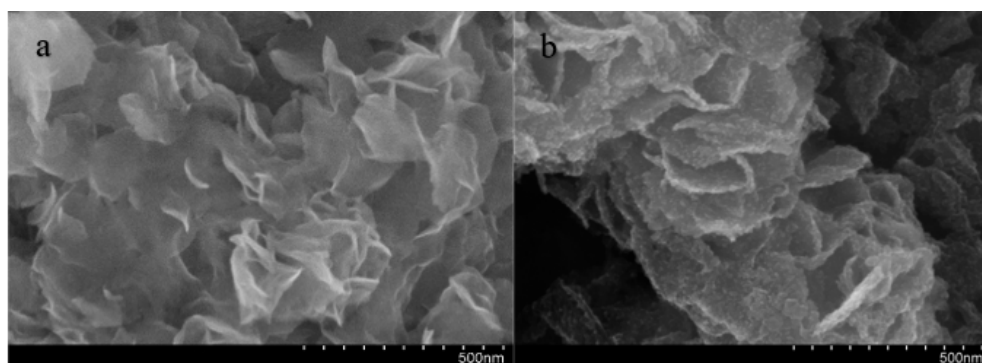


Figure 6. SEM images of (a) MoS₂ nanosheets and (b) MoS₂/ZnO nanomaterials.

3.3. Coating Hydrophobicity Detection

The CA of the MoS₂ nanomaterials was 138.6° (Figure 7a), and the CA of the MoS₂/ZnO nanomaterials was 150.7° (Figure 7b). The uncoated GFRP blades had a CA of 62.3° (Figure 7c), and the CA of the GFRP blades coated with PDMS was 109.8° (Figure 7d), which is lower than the 140.8° for the GFRP coated with the MoS₂/PDMS nanomaterial (Figure 7e), making it a hydrophobic material. When coated with the MoS₂/ZnO/PDMS nanomaterial, the CA and sliding angle (SA) of the coating surface and the water reached 152.1° (Figure 7f) and 4.7°, respectively, indicating that the MoS₂/ZnO/PDMS nano-coating contributed to a superhydrophobic state. The above results show that PDMS, as a binder, has certain hydrophobicity, and the surface hydrophobicity of the coating is mainly affected by the surface characteristics of the MoS₂ and MoS₂/ZnO nanomaterials. Since water droplets fell on the surface of the porous and rough MoS₂/ZnO/PDMS nano-coating, air was trapped in the voids of the layered rough structure surface to form a solid-liquid-gas three-phase contact state. The resulting layer of air cushion between the liquid and the coating surface prevented water droplets from penetrating the porous coating surface. Hydrophobicity can be determined using the Cassie-Baxter wetting model [32]:

$$\cos \theta = f_1(\cos \theta_1 + 1) - 1 \quad (3)$$

where θ is the CA between the MoS₂/ZnO/PDMS nano-coating and the water droplets, θ_1 is the CA between the water droplets and the uncoated GFRP surface, and f_1 is the contact fraction of water droplets and MoS₂/ZnO/PDMS nano-coating surface solids.

Using this formula, the solid contact fraction on the surface of the MoS₂/ZnO/PDMS nano-coating was 7.93%, which means that the contact of the MoS₂/ZnO/PDMS nano-coating with water droplets created a 92.07% air retention area. This shows that the surface of the MoS₂/ZnO/PDMS nano-coating had a superhydrophobic coating property with a layered rough structure surface, which is consistent with the SEM results. Therefore, the coating surface roughness provided by the micro-nano structure contributes significantly to superhydrophobicity.

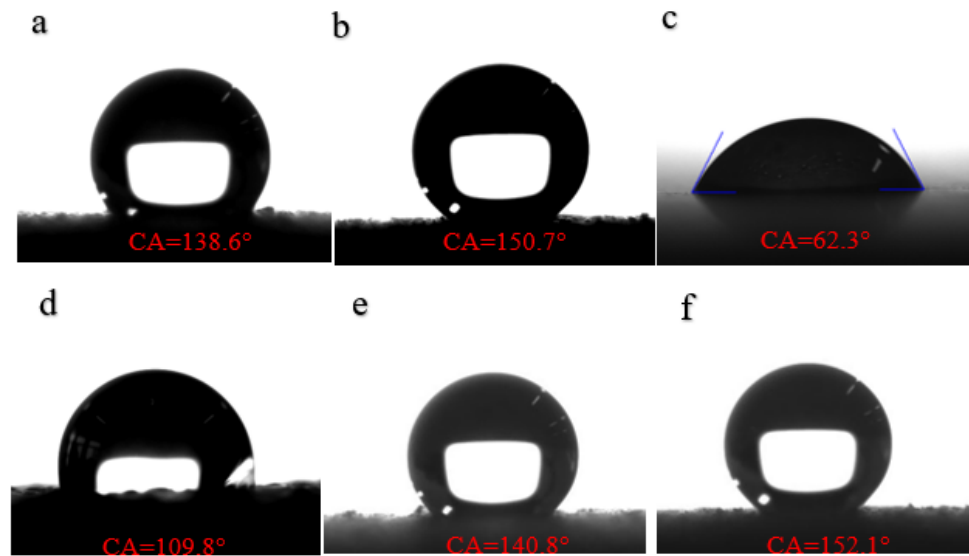


Figure 7. The CA of (a) MoS₂, (b) MoS₂/ZnO, (c) no coating, (d) PDMS coating, (e) MoS₂/PDMS coating, and (f) MoS₂/ZnO/PDMS coating.

The CA of the MoS₂/ZnO/PDMS nanomaterial coatings was tested at different ambient temperatures, and the test results are shown in the Figure 8. As the figure demonstrates, the ambient temperature has an impact on the coating of MoS₂/ZnO/PDMS nanomaterials. At low temperatures, the surface CA decreases, which affects the surface hydrophobicity of the coating.

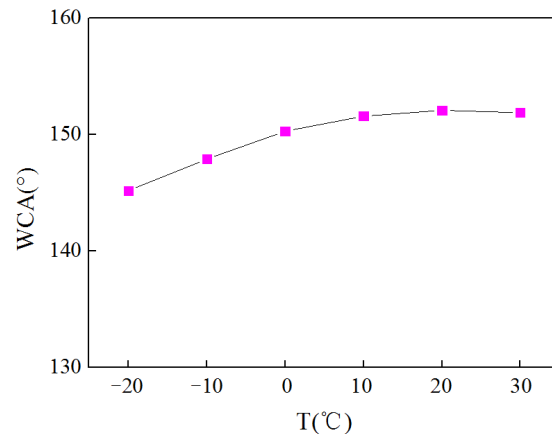


Figure 8. Different ambient temperature MoS₂/ZnO/PDMS coating surface hydrophobic angles.

3.4. Abrasion Resistance Test of Coating

The abrasion resistance of the MoS₂/ZnO/PDMS nano-coatings was tested by placing the coatings on 800 grit sandpaper, using a 100 g weight as a load, and pulling the substrate at a constant rate. In each wear cycle, a lateral movement of 10 cm and a longitudinal movement of 10 cm were guaranteed to ensure non-directional wear.

The wear resistance of the coating is shown in the Figure 9. After 7 wear cycles, the CA of the surface of the MoS₂/ZnO/PDMS nano-coating decreased to 147.3°. It may be that the nano particles on the surface of the coating were easily rubbed off in the early wear, and the rough structure was slightly damaged in the process of the coating wear. The CA of the MoS₂/ZnO/PDMS nanomaterial surface was stable at 145.5°, which indicates that the coating had formed a stable wear-resistant structure, and the MoS₂/ZnO/PDMS nanomaterial exhibited wear-resistant properties.

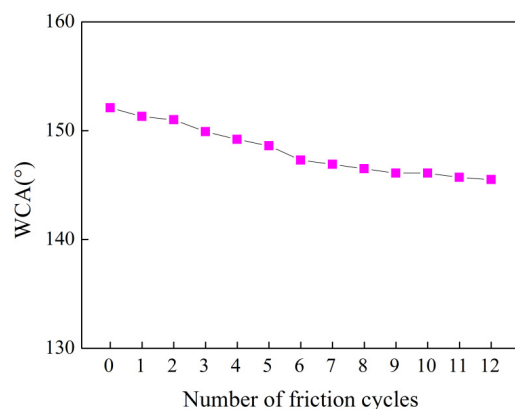


Figure 9. Abrasion resistance coating test surface CAs.

3.5. Icing Adhesion Strength of the Coating

As hydrophobic coating surfaces will still be frozen in environments with low temperatures and high humidity, the adhesion between the ice and the coating is the key to anti-icing. If the adhesion between the ice layer and the coating is low, the ice layer will easily be detached from the coating surface under external forces such as wind and gravity. As demonstrated in Figure 10, the adhesion strengths of ice on the surfaces of the MoS₂/PDMS nano-coating and the MoS₂/ZnO/PDMS nano-coating were 103 kPa and 78 kPa, respectively, which were much lower than the 196 kPa on the uncoated surface. This is because the MoS₂/ZnO/PDMS nano-coating conferred superhydrophobicity. In addition, the micro-nano rough structure on the surface formed a stable Cassie-Baxter state air cushion at the contact interface of the water droplets. After icing, the contact area was smaller compared with the uncoated surface, resulting in less adhesion strength of the ice on the coating surface.

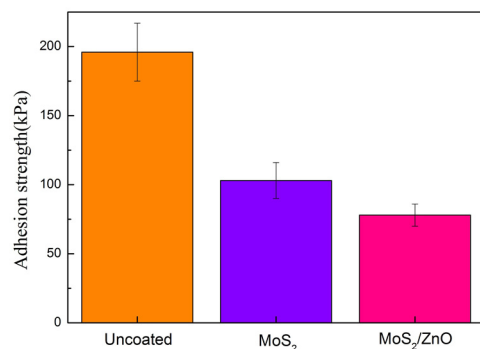


Figure 10. Adhesion strength of ice on GFRP, MoS₂/PDMS, and MoS₂/ZnO/PDMS nano-coating surfaces.

3.6. Chemical Reagent Stability

Superhydrophobic coatings may be exposed to various complex environments (such as acid rain) during practical outdoor applications, which degrades the hydrophobicity of the coatings. Therefore, the chemical stability of superhydrophobic coating was studied. The MoS₂/ZnO/PDMS nano-coating was immersed in different pH solutions for 30 min, and the CA of the coating surface was measured. As demonstrated in Figure 11, the prepared MoS₂/ZnO/PDMS nano-coating had acid and alkali stability. In comparison, the tolerance of the MoS₂/ZnO/PDMS nano-coating to acidic conditions was worse than that of alkaline conditions. The reason is that under acid conditions, the surface ZnO in the MoS₂/ZnO/PDMS nano-coating will react with acid via a metathesis reaction, destroying the original hydrophobic structure of the coating surface and, thereby, reducing the hydrophobic properties of the MoS₂/ZnO/PDMS nano-coating. The acid solution was

measured by an atomic fluorescence photometer, which showed that there was Zn in the solution, which also verified that the ZnO reacted with the acid solution.

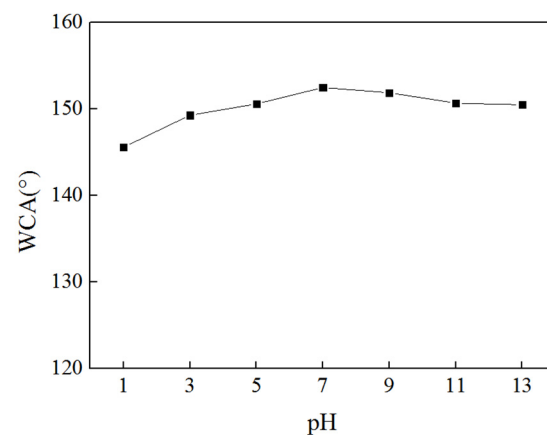


Figure 11. The CA of coating surfaces soaked in different pH solution for 30 min.

3.7. Icing Distribution on Blade Surface

The icing test results for the uncoated GFRP blade, the MoS₂/PDMS nanomaterial-coated GFRP blade, and the MoS₂/ZnO/PDMS nanomaterial-coated GFRP blade at $-10\text{ }^{\circ}\text{C}$, 5 m/s and $-15\text{ }^{\circ}\text{C}$, 10 m/s for 3 min are shown in Figure 12.

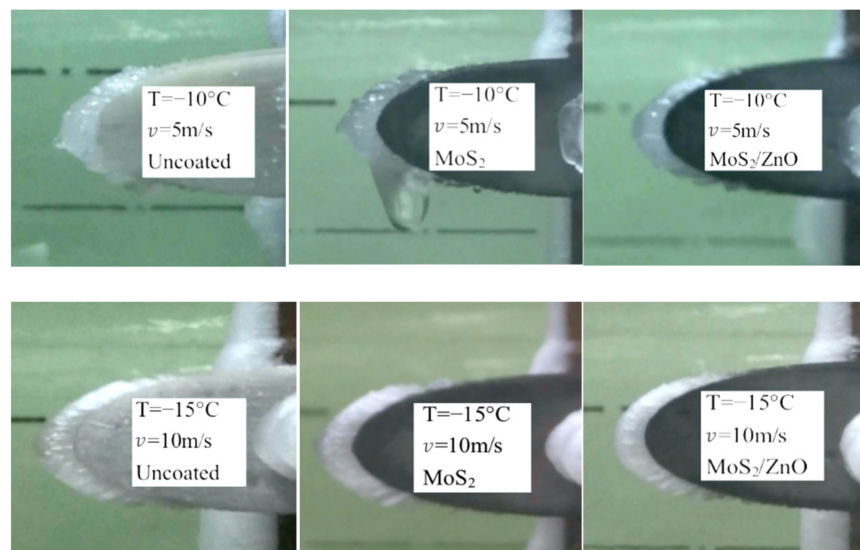


Figure 12. Icing wind tunnel test variables.

A blade surface icing contour map was generated for each of the uncoated GFRP blade, the MoS₂/PDMS nanomaterial-coated GFRP blade, and the MoS₂/ZnO/PDMS nanomaterial-coated GFRP blade to measure the blade surface icing shape at 3 min using digital processing. As demonstrated in Figure 13, icicles appeared on the lower surface of the leading edge of the blade in tests 1, 2, and 4. This change can be attributed to the difference in thermal conductivity between the ice layer and the GFRP blade. The thermal conductivity of the ice layer was $2.2\text{ W}/(\text{m}\cdot\text{K})$, while the thermal conductivity of the GFRP blade was $0.42\text{ W}/(\text{m}\cdot\text{K})$. As a result, when the supercooled water droplets were blown to the blade surface at high temperatures or low wind speeds, the time required for the supercooled water droplets to reach the thermal equilibrium between the supercooled water droplets and the blade increased, resulting in the freezing of the supercooled water droplets. Under the combined action of airflow and gravity, the unfrozen water droplets flowed downward and accumulated to form an ice column. In the other tests, when the

ambient temperature as low or the wind speed was high, heat transfer was accelerated, and the time required to achieve a heat balance between supercooled water drops and the blade surface was reduced, the time required for freezing was reduced, and no icicle was generated at the leading edge of blade.

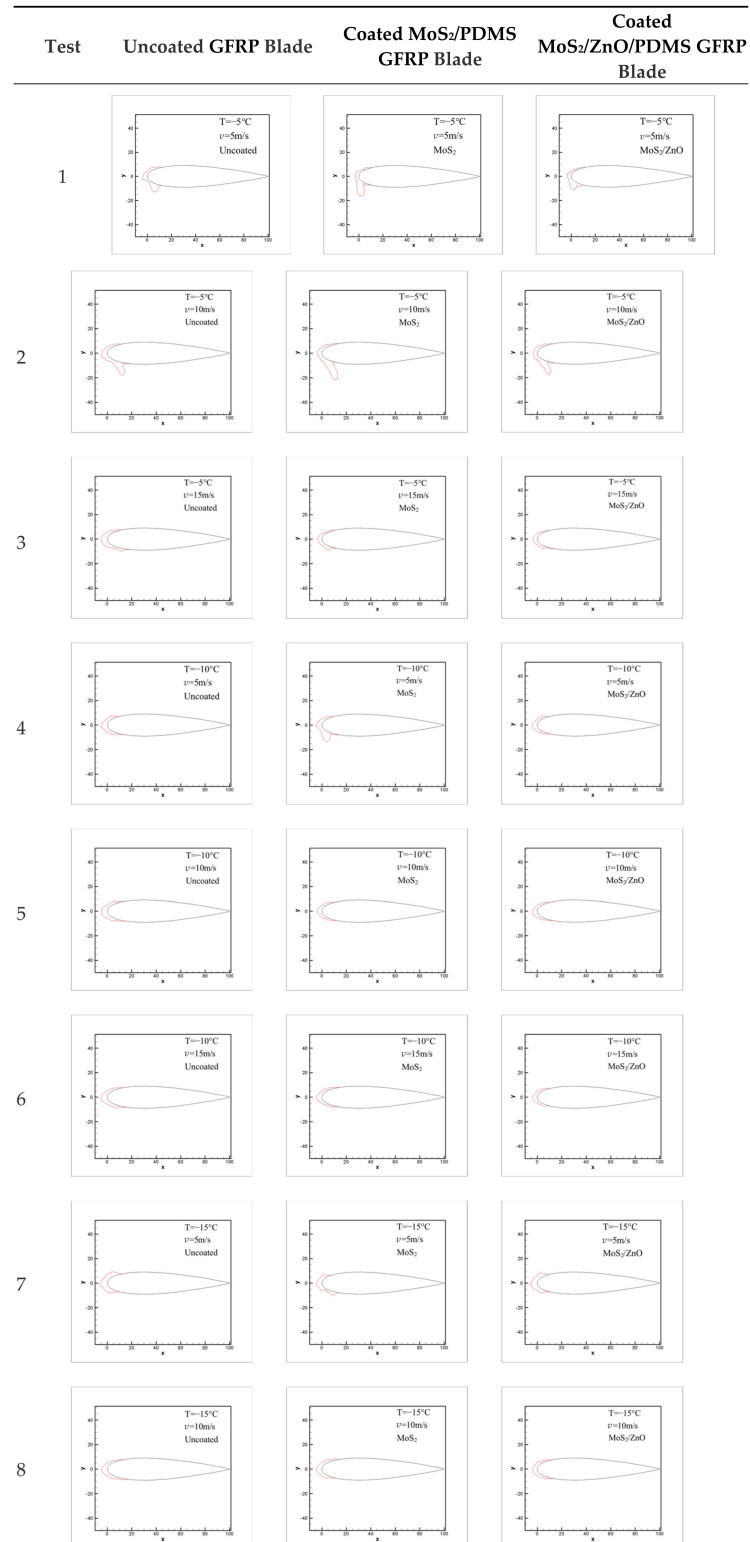


Figure 13. Cont.

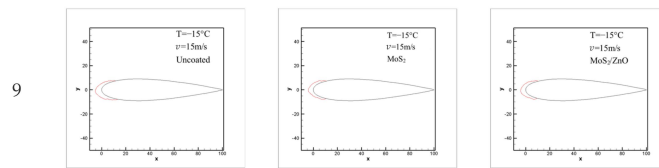


Figure 13. Icing profiles of blade surface in different environments.

3.8. The Effect of Ambient Temperature on Icing Distribution

To explore the anti-icing properties of the MoS₂/ZnO/PDMS nanomaterial coating at the same wind speed and different temperatures, the uncoated GFRP blade, the MoS₂/PDMS-coated GFRP blade, and the MoS₂/ZnO/PDMS-coated GFRP blade were selected to explore the thickness of the ice layer at the leading edge of the blade and the icing area at the leading edge of the blade at $-5\text{ }^{\circ}\text{C}$, $-10\text{ }^{\circ}\text{C}$, and $-15\text{ }^{\circ}\text{C}$ ambient temperatures with wind speeds of 10 m/s.

The data shown in Figure 14a reveal that at the same wind speed, the ice thickness at the leading edge of the blade increased with the decrease in ambient temperature. At $-5\text{ }^{\circ}\text{C}$, $-10\text{ }^{\circ}\text{C}$, and $-15\text{ }^{\circ}\text{C}$ ambient temperatures and wind speeds of 10 m/s the icing thickness of the leading edge of the blades coated with MoS₂/ZnO/PDMS nanomaterials decreased by 20.4%, 13.7%, and 18.5%, respectively. This is because, compared with the uncoated blade, the contact angle of the blade surface coated with the hydrophobic coating increased, the adhesion force of the water droplets on the blade surface decreased, and the water droplets slid down under the action of airflow and gravity, which reduced the freezing of water droplets on the leading edge of the blade. Therefore, the leading-edge icing thickness of the blade coated with MoS₂/ZnO/PDMS nanomaterials was thinner than that of the blade coated with MoS₂/PDMS nanomaterials and the uncoated blade.

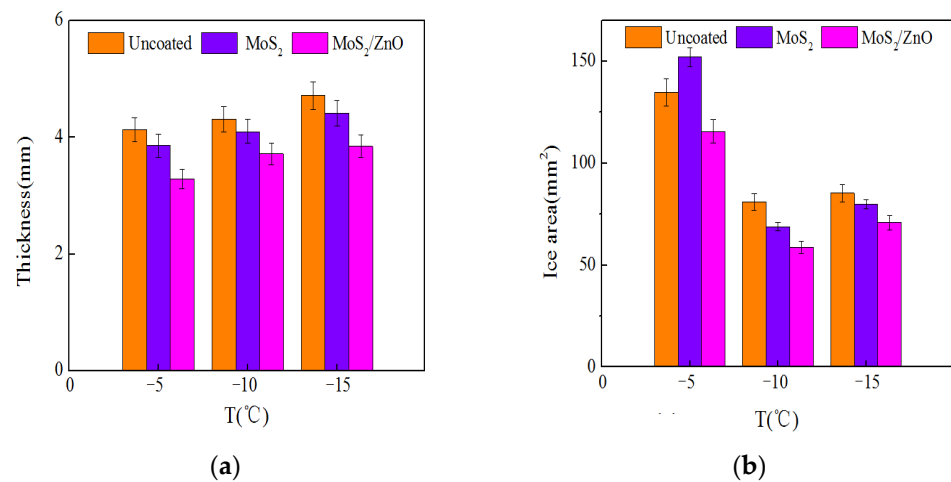


Figure 14. Icing conditions of blade leading edges coated with different materials under various ambient temperatures and at wind speeds of 10 m/s: (a) icing thickness (b) icing area.

Figure 14b shows the icing area of the leading edge of the blade at different ambient temperatures at wind speeds of 10 m/s. Notably, the icing area of the leading edge of the blade coated with the MoS₂/ZnO/PDMS nanomaterials was the smallest among the materials under the same conditions. At $-5\text{ }^{\circ}\text{C}$, $-10\text{ }^{\circ}\text{C}$, and $-15\text{ }^{\circ}\text{C}$ ambient temperatures and wind speeds of 10 m/s, the icing area of the MoS₂/ZnO/PDMS nanomaterial-coated blade decreased by 14.2%, 28.3%, and 16.9%, respectively, compared with the uncoated blade. At a wind speed of 10 m/s and a $-5\text{ }^{\circ}\text{C}$ environment, the ice column and surface icing area of the leading edge of the blade that was coated with MoS₂/PDMS nanomaterial were larger than those of the uncoated blade and the blade coated with the MoS₂/ZnO/PDMS nanomaterial. This may be explained by the hydrophilic nature of the uncoated blade, the

strong adhesion between water droplets and the blade, and the ease with which water droplets rolled off, whereas the MoS_2/PDMS nanomaterial is a hydrophobic coating, and the water droplets flowed downward under the combined action of airflow and gravity but did not reach the superhydrophobic state. This made it difficult for water droplets to flow quickly, resulting in longer icicles at the leading edge of the blade.

3.9. Influence of Wind Speed on Icing Distribution

Figure 15 shows the ice thickness and icing area of the leading edge of the blade under the temperature of $-10\text{ }^\circ\text{C}$ and various wind speeds for 3 min. The results demonstrated that under the same conditions, the icing thickness and icing area of the leading edge of the blade without a hydrophobic coating were larger than those of the blade coated with the $\text{MoS}_2/\text{ZnO}/\text{PDMS}$ nanomaterials. The icing thickness of the leading edge of the MoS_2/PDMS nanomaterial-coated blade was increased at the wind speed of 5 m/s. This is because at a lower wind speed, the supercooled water droplets were not significantly affected by the airflow after hitting the blade surface, and the ice layer concentrated around the leading edge of the blade. Under the combined action of gravity and superhydrophobic properties, unfrozen water droplets began to flow downward to form icicles. The surface of the blade became irregular, the aerodynamic shape of the blade was damaged, and the thickness of the leading edge of the blade and the icing area of the leading edge increased.

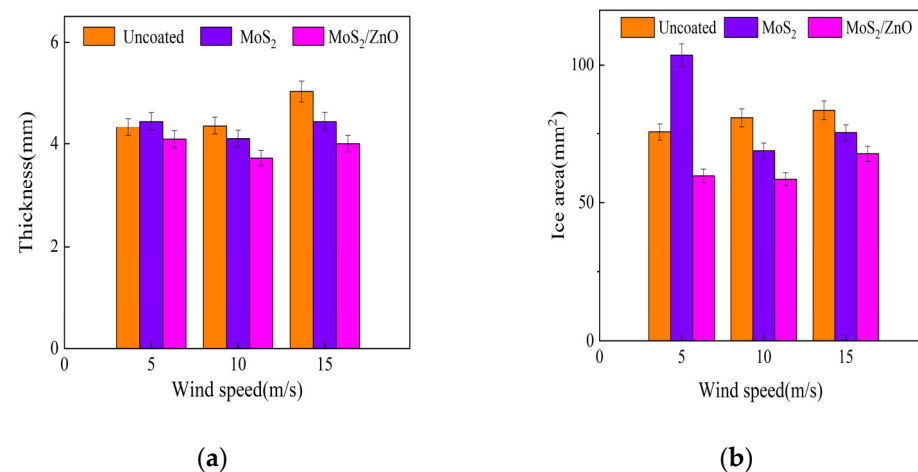


Figure 15. Icing conditions of blade leading edges coated with different materials at $-10\text{ }^\circ\text{C}$ ambient temperatures with various wind speeds: (a) icing thickness (b) icing area.

4. Conclusions

- (1) In this study, MoS_2/ZnO nano-superhydrophobic material with nano-rough structure on the surface was prepared using the hydrothermal method and the liquid phase method. The surface formed a micro-nano rough structure which was used to construct a superhydrophobic surface. The CA was 152.1° , and the SA was 4.7° .
- (2) The surface of the $\text{MoS}_2/\text{ZnO}/\text{PDMS}$ nano-superhydrophobic coating was porous and rough and formed a layer of air cushion in contact with liquid, which reduced the adhesion between liquids and the coating surface, thereby reducing the adhesion strength between the coating and ice.
- (3) The icing wind tunnel test showed that the $\text{MoS}_2/\text{ZnO}/\text{PDMS}$ nanomaterial-coated blade had lower amounts of icing than the uncoated blade under the same conditions. The icing thickness of the leading edge of the blade was decreased by up to 20.4%, and the icing area was reduced by about 28.3%.

This study provides a reference for the design of wind turbine blade anti-icing coatings and contributes to improving anti-icing technology.

Author Contributions: Conceptualization, B.L., Y.L. and F.F.; formal analysis, B.L., Y.L. and F.F.; funding acquisition, F.F.; investigation, B.L. and Z.L.; methodology, B.L. and Z.L.; supervision, Y.L. and F.F.; validation, Z.L. and Y.L.; writing—original draft, B.L.; writing—review and editing, Z.L., Y.L. and F.F. All authors have read and agreed to the published version of the manuscript.

Funding: This work was supported by project grant No. 52076035 from the National Natural Science Foundation of China (NSFC) and provided with project grant No. IADL20200405 from the Open Fund of Key Laboratory of Icing and Anti-/De-Icing, China Aerodynamics Research and Development Center.

Institutional Review Board Statement: Not applicable.

Informed Consent Statement: Not applicable.

Data Availability Statement: Not applicable.

Conflicts of Interest: The authors declare no conflict of interest.

References

1. Li, Y.; Shen, H.; Guo, W. Simulation and experimental study on the ultrasonic micro-vibration Deicing method for wind turbine blades. *Energies* **2021**, *14*, 8246. [[CrossRef](#)]
2. Guo, W.; Shen, H.; Li, Y.; Feng, F.; Tagawa, K. Wind tunnel tests of the rime icing characteristics of a straight-bladed vertical axis wind turbine. *Renew. Energy* **2021**, *179*, 116–132. [[CrossRef](#)]
3. Tong, G.; Li, Y.; Tagawa, K.; Feng, F. Effects of blade airfoil chord length and rotor diameter on aerodynamic performance of straight-bladed vertical axis wind turbines by numerical simulation. *Energy* **2023**, *265*, 126325. [[CrossRef](#)]
4. Rashidi, M.M.; Mahariq, I.; Murshid, N.; Wongwises, S.; Mahian, O.; Nazari, M.A. Applying wind energy as a clean source for reverse osmosis desalination: A comprehensive review. *Alex. Eng. J.* **2022**, *61*, 12977–12989. [[CrossRef](#)]
5. Zheng, C.W.; Li, C.Y.; Pan, J.; Liu, M.Y.; Xia, L.L. An overview of global ocean wind energy resource evaluations. *Renew. Sustain. Energy Rev.* **2016**, *53*, 1240–1251. [[CrossRef](#)]
6. Caccia, F.; Guardone, A. Numerical simulation of ice accretion on wind turbine blades. *Wind Energy Sci. Discuss.* **2023**, *8*, 341–362. [[CrossRef](#)]
7. Guo, W.; Zhang, Y.; Li, Y.; Tagawa, K.; Zhao, B. A Wind Tunnel Experimental Study on the Icing Characteristics of a Cylinder Rotating around a Vertical Axis. *Appl. Sci.* **2021**, *11*, 10383. [[CrossRef](#)]
8. Jiang, F.; Qiu, T. Research on the effect of icing on aerodynamic performance of airfoil and power generation performance of wind turbine. *J. Phys. Conf. Ser.* **2020**, *1684*, 012141. [[CrossRef](#)]
9. Chen, J.; Luo, Z.; An, R.; Marklund, P.; Björling, M.; Shi, Y. Novel Intrinsic Self-Healing Poly-Silicone-Urea with Super-Low Ice Adhesion Strength. *Small* **2022**, *18*, 2200532. [[CrossRef](#)]
10. Liu, Z.; Feng, F.; Li, Y.; Sun, Y.; Tagawa, K. A corn cob biochar-based superhydrophobic photothermal coating with micro-nano-porous rough-structure for ice-phobic properties. *Surf. Coat. Technol.* **2023**, *457*, 129299. [[CrossRef](#)]
11. Liao, C.; Yi, Y.; Chen, T.; Cai, C.; Deng, Z.; Song, X.; Lv, C. Detecting Broken Strands in Transmission Lines Based on Pulsed Eddy Current. *Metals* **2022**, *12*, 1014. [[CrossRef](#)]
12. Mu, Z.; Li, Y.; Guo, W.; Shen, H.; Tagawa, K. An Experimental Study on Adhesion Strength of Offshore Atmospheric Icing on a Wind Turbine Blade Airfoil. *Coatings* **2023**, *13*, 164. [[CrossRef](#)]
13. Li, L.; Liu, Y.; Tian, L.; Hu, H.; Hu, H.; Liu, X.; Hogate, I.; Kohli, A. An experimental study on a hot-air-based anti-/de-icing system for aero-engine inlet guide vanes. *Appl. Therm. Eng.* **2020**, *167*, 114778. [[CrossRef](#)]
14. Li, Y.; Shen, H.; Guo, W. Effect of ultrasonic vibration on the surface adhesive characteristic of iced Aluminum alloy plate. *Appl. Sci.* **2022**, *12*, 2357. [[CrossRef](#)]
15. He, Z.; Xie, H.; Jamil, M.I.; Li, T.; Zhang, Q. Electro-/Photo-Thermal Promoted Anti-Icing Materials: A New Strategy Combined with Passive Anti-Icing and Active De-Icing. *Adv. Mater. Interfaces* **2022**, *9*, 2200275. [[CrossRef](#)]
16. Liu, Y.; Zhao, Z.; Shao, Y.; Wang, Y.; Liu, B. Preparation of a superhydrophobic coating based on polysiloxane modified SiO₂ and study on its anti-icing performance. *Surf. Coat. Technol.* **2022**, *437*, 128359. [[CrossRef](#)]
17. Rivero, P.J.; Rodriguez, R.J.; Larumbe, S.; Montesión, M.; Martín, F.; García, A.; Acosta, C.; Clemente, M.J.; García, P.; Mora, J.; et al. Evaluation of functionalized coatings for the prevention of ice accretion by using icing wind tunnel tests. *Coatings* **2020**, *10*, 636. [[CrossRef](#)]
18. Zhang, L.; Chen, C.; Zhou, J.; Yang, G.; Wang, J.; Liu, D.; Chen, Z.; Lei, W. Solid phase exfoliation for producing dispersible transition metal dichalcogenides nanosheets. *Adv. Funct. Mater.* **2020**, *30*, 2004139. [[CrossRef](#)]
19. Yang, J.; Xiao, Q.; Lin, Z.; Li, Y.; Jia, X.; Song, H. Growth of ultra-dense MoS₂ nanosheets on carbon fibers to improve the mechanical and tribological properties of polyimide composites. *Friction* **2021**, *9*, 1150–1162. [[CrossRef](#)]
20. Zhang, X.; Wang, H.; Zhang, X.; Zhao, Z.; Zhu, Y. A multifunctional super-hydrophobic coating based on PDA modified MoS₂ with anti-corrosion and wear resistance. *Colloids Surf. A Physicochem. Eng. Asp.* **2019**, *568*, 239–247. [[CrossRef](#)]
21. Klingshirn, C. ZnO: Material, physics and applications. *ChemPhysChem* **2007**, *8*, 782–803. [[CrossRef](#)] [[PubMed](#)]

22. Saiduzzaman, M.; Takei, T.; Kumada, N. Hydrothermal magic for the synthesis of new bismuth oxides. *Inorg. Chem. Front.* **2021**, *8*, 2918–2938. [[CrossRef](#)]
23. Ma, X.; Zhuang, J.; Zhao, P.; Zhang, H.; Li, H.; Xie, J.; Rong, J.; Ding, Y.; Wang, G. Hydrothermal synthesis and electrical properties of Co–Mn–Fe–Zn–O NTC nanopowder materials. *J. Mater. Sci. Mater. Electron.* **2021**, *32*, 25201–25213. [[CrossRef](#)]
24. Wang, Y.; Yan, L.; Ling, Y.; Ge, Y.; Huang, C.; Zhou, S.; Xia, S.; Liang, M.; Zou, H. Enhanced mechanical and adhesive properties of PDMS coatings via in-situ formation of uniformly dispersed epoxy reinforcing phase. *Prog. Org. Coat.* **2023**, *174*, 107319. [[CrossRef](#)]
25. Hong, S.; Wang, R.; Huang, X.; Liu, H. Facile one-step fabrication of PHC/PDMS anti-icing coatings with mechanical properties and good durability. *Prog. Org. Coat.* **2019**, *135*, 263–269. [[CrossRef](#)]
26. Dhiman, V.; Kondal, N. MoS₂–ZnO nanocomposites for photocatalytic energy conversion and solar applications. *Phys. B Condens. Matter* **2022**, *628*, 413569. [[CrossRef](#)]
27. Shi, L.; Feng, F.; Guo, W.; Li, Y. Research and development of a small-scale icing wind tunnel test system for blade airfoil icing characteristics. *Int. J. Rotating Mach.* **2021**, *2021*, 5598859. [[CrossRef](#)]
28. Selvaraj, R.; Kalimuthu, K.R.; Kalimuthu, V. A type-II MoS₂/ZnO heterostructure with enhanced photocatalytic activity. *Mater. Lett.* **2019**, *243*, 183–186. [[CrossRef](#)]
29. Krishnan, U.; Kaur, M.; Kaur, G.; Singh, K.; Dogra, A.R.; Kumar, M.; Kumar, A. MoS₂/ZnO nanocomposites for efficient photocatalytic degradation of industrial pollutants. *Mater. Res. Bull.* **2019**, *111*, 212–221. [[CrossRef](#)]
30. Xu, X.; Wang, S.; Liu, W.; Chen, Y.; Ma, S.; Yun, P. An excellent triethylamine (TEA) sensor based on unique hierarchical MoS₂/ZnO composites composed of porous microspheres and nanosheets. *Sens. Actuators B Chem.* **2021**, *333*, 129616. [[CrossRef](#)]
31. Liu, H.Q.; Yao, C.B.; Jiang, C.H.; Wang, X. Preparation, modification and nonlinear optical properties of semiconducting MoS₂ and MoS₂/ZnO composite film. *Opt. Laser Technol.* **2021**, *138*, 106905. [[CrossRef](#)]
32. Yan, W.; Sun, J.; Golsanami, N.; Li, M.; Cui, L.; Dong, H.; Sun, Y. Evaluation of wettabilities and pores in tight oil reservoirs by a new experimental design. *Fuel* **2019**, *252*, 272–280. [[CrossRef](#)]

Disclaimer/Publisher’s Note: The statements, opinions and data contained in all publications are solely those of the individual author(s) and contributor(s) and not of MDPI and/or the editor(s). MDPI and/or the editor(s) disclaim responsibility for any injury to people or property resulting from any ideas, methods, instructions or products referred to in the content.